High Resolution Sea Ice Motion Estimation With Optical Flow Using Satellite Spectroradiometer Data

Zisis I. Petrou, *Member, IEEE,* and YingLi Tian, *Senior Member, IEEE*

***Abstract*—The purpose of this study is twofold: First, to propose an approach based on optical flow for the estimation of sea ice motion as an accurate, dense, and computationally efficient alternative to state-of-the-art pattern matching approaches. Second, to investigate the potential of MODIS optical satellite data for combined daily and high resolution motion estimation. A series of MODIS image pairs for a selected region in Arctic Ocean are employed and sparse pairwise correspondences between non-rigid patches are calculated. An edge preserving sparse-to-dense interpolation is applied followed by variational energy minimization to compute the final optical flow. A state-of-the-art multi-resolution pattern-matching method based on phase correlation and normalized cross-correlation is also implemented and evaluated for comparison. Thorough experimentation with different settings of input data pre-processing as well as varying scales of motion is performed. The derived motion vectors are compared with coarser resolution operational sea ice motion vector products from combined buoy and microwave satellite data. The proposed optical flow approach clearly outperforms the pattern matching method in most cases, both in terms of accuracy and motion vector consistency. The estimated motion vectors from the MODIS images correlate highly with the operational vector products. In addition, MODIS provides a vector field with spatial resolution two orders of magnitude higher than the operational products that is able to detect significantly smaller sea ice drifts.**

***Index Terms*—Arctic sea ice, dense matching, EpicFlow, hierarchical maximum cross correlation, Moderate Resolution Imaging Spectroradiometer (MODIS), motion tracking, motion vectors, optical flow, phase correlation, sea ice drift estimation.**

I. Introduction

SEA ice motion is a crucial component in climate studies. On a large (e.g., pan-Arctic) scale, estimation of sea ice motion is necessary to quantify ice volume exchanges and to understand the exchange of energy, momentum, and mass between the ocean and the atmosphere [1]. It has been used to validate or improve models predicting polar ice pack conditions [2]–[4]. Between 1973 and 2003, the annual average sea ice extent in the Arctic decreased by around 8% [5]. Reduced sea ice extent is expected to increase sea ice motion. In fact, an average increase on the Arctic sea ice drift speed by 10.6% $\pm$ 0.9% per decade was observed for the period 1992–2009, significantly larger than the wind speed increase of around 1.5% per decade for the same period [6]. Besides on a regional scale, such increase can also have profound effects on a local scale, affecting or putting in danger ship navigation, oil and gas exploration, and fisheries. Thus, information on sea ice motion is required on a daily basis and at a relatively high spatial resolution [7], [8].

A variety of remote sensing data have been used for sea ice motion estimation. Data from passive microwave satellite sensors have been among the most widely employed in research studies [4], [8]–[12] and operational sea ice motion products [13], [14]. The main rationale is their independence from cloud and sun illumination conditions, which allows all-year coverage, and their extended swath width of around 1400 km, which permits multiple satellite passes over the Polar regions, thus, daily coverage. Microwave scatterometers share similar properties and have also been employed in several studies [15]–[17]. However, the coarse spatial resolution of both passive microwave sensors and scatterometers (typically between 6.25 km and 25 km) hinders their applicability in local scale conditions, e.g., for naval operations. On the contrary, Synthetic Aperture Radar (SAR) data, combining weather- and sunlight-independent monitoring potential with high spatial resolution typically ranging between 25 and 400 m, have been extensively applied in sea ice motion estimation [18]–[25]. However, their relatively narrow swath width restricts repeat coverage of Arctic regions to approximately three days [4], [14]. In addition to the previous data, passive optical sensor imagery, in particular from the Advanced Very High Resolution Radiometer (AVHRR), has also been employed in sea ice motion studies [26], [27] as well as in operational products, such as from the National Snow and Ice Data Center (NSIDC) [13]. The high sensitivity to clouds and high atmospheric water presence, especially during summer months of high ice melt and evaporation, and the need for sun light, which hinders its applicability in several polar regions during the mid-winter, may limit their use. On the other hand, desirable properties include their wide swath providing daily coverage and their higher spatial resolution than the passive microwave sensors. However, the spatial resolution of AVHRR still remains in the order of some kilometers (typically 1.1–5 km), with little usefulness for local-scale applications.

The majority of the existing sea ice motion estimation approaches have been based on pattern matching. Let two geolocated images from the same area but captured in different time, usually within a single- or multi-day interval, be used as input. Then, for a specific subregion of the first image, or a *template*, the approaches search within the second image to find the subregion which best matches the pattern of the former

Manuscript submitted August 6, 2016. Revision submitted September 22, 2016. This work was supported in part by ONR grant N000141310450.

Z. I. Petrou is with the Department of Electrical Engineering, The City College of New York, The City University of New York, New York, NY, 10031 USA, e-mail: zpetrou@ccny.cuny.edu.

Y. Tian is with the Department of Electrical Engineering, The City College of New York and the Department of Computer Science, The Graduate Center, The City University of New York, New York, NY, 10031 USA phone: +1-212-650-7046; fax: +1-212-650-8249; e-mail: ytian@ccny.cuny.edu.

one based on a specified evaluation measure. The Euclidean distance between the two subregions indicates the motion of the template, e.g., sea ice floes, from the first image to the second. The most widely adopted template matching measure for sea ice motion estimation has been the normalized cross-correlation (NCC) [4], [8], [10], [12]–[14], [17], [26], [27], whereas more recent studies have employed phase correlation (PC), either in combination with NCC or alone [20]–[25]. Pattern matching approaches are relatively easy to implement and have been able to capture translational, and to a lesser degree, rotational motions. However, their applicability in non-rigid transformations has been limited, whereas they often result in a non-dense motion vector field of coarser spatial resolution than the employed data.

This study has two main contributions. First, we propose an optical flow approach with prior generation of sparse correspondences between two images to provide sea ice motion estimation. Optical flow has been applied in sea ice motion before, but in a small number of studies, since its potential in capturing large displacements has been considered limited [20]. However, comparison of the proposed optical flow approach with a state-of-the-art pattern matching approach shows that the former outperforms the latter under both small and large sea ice drifts, while providing a neighborhood-consistent and dense motion vector field at the resolution of the original images. The second contribution of our paper is to explore the use of optical Moderate Resolution Imaging Spectroradiometer (MODIS) data for sea ice motion estimation. To the best of our knowledge this is the first time MODIS data are employed in sea ice motion studies. Despite the common availability limitations of optical data, MODIS imagery shows capable in providing sea ice motion vectors that i) combine a spatial resolution similar to SAR data with the daily coverage from AVHRR and passive microwave sensors, and ii) highly correlate with operational sea ice motion products from buoys, AVHRR, and passive microwave data [13].

The manuscript is structured as follows. Section II presents related work on sea ice motion estimation with satellite data. Section III refers to the selection and processing of the employed data, whereas the methods proposed are described in Section IV. Results of the experiments and discussions on the outcomes are drawn in Sections V and VI, respectively. Concluding remarks are provided in Section VII.

II. Related work

A. Pattern Matching Approaches

Pattern matching (or *template* or *area-based* or *block* matching) approaches have been the most widely adopted ones in sea ice motion estimation. Under this category, methodologies based on maximum cross-correlation (MCC) have been among the oldest and mostly employed. Starting to be used from the early stages of satellite data in meteorological applications [28], MCC-based approaches have been employed in sea ice motion estimation since the mid 1980's [26]. For a specific template (subregion) in an image, the approaches search for the template in a second image that maximizes the cross-correlation with the former one. The most commonly used evaluation measure is the normalized cross correlation, calculated as [29]:

$$NCC(u_x, u_y) = \frac{cov[A(x,y), B(x+u_x, y+u_y)]}{\sigma[A(x,y)]\sigma[B(x+u_x, y+u_y)]}, \quad (1)$$

where $A(x,y)$ represents the template centered at position (x,y) in the first image, $B(x+u_x, y+u_y)$ a template of the same size centered at ($x+u_x$,$y+u_y$) in the second image, $\sigma(A)$ and $\sigma(B)$ stand for the standard deviation of the pixel values of the templates A and B, respectively, $cov(A,B)$ for the covariance between A and B, and $\boldsymbol{u} = (u_x, u_y)$ represents the displacement of the template, i.e., the *motion vector*. The motion vector is often expressed as velocity, dividing the drift by the respective time period of the motion. The normalization by $\sigma(A)\sigma(B)$ in (1) is used to make NCC illumination invariant, i.e., decrease the sensitivity of the method to small intensity variations between the pair images. In some studies where the standard deviation of the images has been assumed constant, the normalization term is omitted in order to face the measure as convolution and calculate it faster in the Fourier domain. However, most studies adopt the normalization term to increase robustness to such variations and calculate NCC in the spatial domain with the expense of higher computation time.

In one of the first MCC approaches, Ninnis *et al.* [26] used visible (0.58–0.68 μm) AVHRR images of 1.7 km to estimate sea ice motion in the Beaufort Sea in non-overlapping templates, i.e., for every 22 pixels, or around 37 km. Emery *et al.* [27] applied filtering out of vectors with NCC value lower than a threshold and vectors deviating from their neighboring ones, and employed overlapping templates, thus, increasing the resolution of the motion vector field to the one of the original AVHRR data. Modifications of this method have been applied to microwave sensors [4], [9], [11], [12] and/or scatterometer data [8], [17] in later studies as well as in current operational sea ice motion vector products [13]. Different approaches have been proposed to increase the resolution of the resulting motion vector field, such as linear oversampling [4], [12] or interpolation in the image data [14] and curve fitting in the correlation value domain [10], with the final resolution, though, remaining in the order of some km. Besides the high computation time when calculated in the spatial domain, another shortcoming of NCC is that it can be used only under the assumption of uniform translational or nearly translational motion [30], thus, cannot handle rotational motion or non-rigid transformations.

Phase correlation (PC) has been introduced in several studies to account for the NCC shortcoming in rotational motion and speed up the calculation process. PC is calculated in the Fourier domain taking advantage of the property that a translational shift in the spatial domain is transformed into a phase shift in the Fourier domain. Having a template A in the first image and a template B in the same location in the second image, the PC matrix is calculated as their normalized cross-power spectrum [23], [25]:

$$PC = \mathcal{F}^{-1}\left(\frac{F_A^* F_B}{|F_A^* F_B|}\right), \quad (2)$$

where F_A^* stands for the conjugate Fourier transform of A, F_B for the Fourier transform of B, and $\mathcal{F}^{-1}$ the inverse Fourier transform operator. The relative motion is estimated from the location in the spatial domain that corresponds to the maximum value of the PC matrix in (2). Thomas *et al.* [20] proposed a multi-resolution approach using PC to pre-select candidate motion vectors and NCC for the final evaluation and selection. European Remote Sensing Satellite-1 (ERS-1) SAR imagery was used with the resulting motion vector field having a resolution of 400 m. A modification using image impainting was later proposed to account for motion estimation close to discontinuous regions [21]. Building on this approach, Hollands and Dierking [22] utilized Envisat Advanced SAR (ASAR) data at 25 m spatial resolution to extract a motion vector field of a resolution of around 300 m. In [23], PC entirely substituted NCC, although not directly providing a clear measure of similarity between two templates [24].

Some studies have combined pattern matching with feature tracking, i.e., identification of matching pixels, patches, or generated features in the two images [24], [25], [31]. In [25], an image pre-processing step, a Fourier-Mellin transform, and a feature tracking approach were combined with multi-resolution pattern matching to capture rotational motion. In [24], candidate translational and rotational motion vectors were estimated through an automated selection of control points employing PC, whereas NCC was employed for the final evaluation. Wavelet analysis has also been used to a lesser degree [15].

B. Optical Flow Approaches

Certain studies on sea ice motion estimation have employed optical flow analysis [16], [18], [19]. Optical flow is a computer vision approach estimating the apparent motion of surfaces, edges, and objects between images. Images are represented as 3D vector fields, $I(x, y, t)$, where (x, y) and t denote the spatial coordinates and time, respectively. For a specific time instance pair of images, the spatial motion, $\boldsymbol{u} = (u_x, u_y)$, is estimated for every pixel. To allow the calculation of the optical flow, a number of assumptions are needed. The most common one is the *brightness constancy assumption* [32], which states that the brightness (intensity) of a pixel remains constant during its motion, and for a specific pixel is expressed as:

$$I_x u_x + I_y u_y + I_t = 0, \tag{3}$$

where I_x, I_y, and I_t denote the partial derivatives of the image function in x axis, y axis, and time, respectively. Equation (3) is under-determined, since only I_x, I_y, and I_t are known, a condition related to the so-called *aperture problem* [32]. Additional constrains need to be introduced to overcome the problem, with the main proposed solutions organized under the feature-based and variational approach categories [33]. The former calculate the optical flow per pixel neighborhood independently of the other pixel neighborhoods in an image, assuming a constant or affine motion per neighborhood. They mainly involve gradient based minimization of the quadratic [34] or absolute [35] deviations shown in (3). The latter approaches impose a motion vector smoothness constraint over the entire image, minimizing an energy by means of variational approaches, as in [36]:

$$\min_{u_x,u_y} \Big[\int_\Omega (I_x u_x + I_y u_y + I_t)^2 \mathrm{d}\Omega + \lambda \int_\Omega (|\nabla u_x|^2 + |\nabla u_y|^2) \mathrm{d}\Omega \Big], \tag{4}$$

where Ω stands for the image domain and $\lambda \in \mathbb{R}$ for a relative weight of the two terms. The first term represents the *data* term, whereas the second the *smoothness* term.

Contrary to pattern matching and feature tracking approaches which mainly provide sparse motion vector fields, optical flow approaches usually provide dense motion fields, i.e., for every pixel of an image pair [18]. Since resulting in individual pixel motion vectors instead of considering the motion of a template as uniform, they can theoretically capture more effectively sea ice deformations, such as ice ridges and leads. In [18] and [19] a power spectrum and cross-correlation techniques are initially applied for a rough estimation on the translational and rotational motion, and then, variational optical flow without the smoothness constraint is applied iteratively to enhance the estimation of the rotational and deformational motion. Feature-based optical flow has been applied in scatterometer data for sea ice motion estimation in [16]. The use of optical flow techniques has been relatively restricted, considered highly sensitive to varying degrees of illumination between images and inaccurate under large or discontinuous displacements because of the inherent smooth constraints applied to counteract the aperture problem [20]. However, optical flow techniques can be calculated, in general, faster than NCC-based methods and provide a dense motion vector field, contrary with some NCC methods where templates move in a multi-pixel step, whereas recent advances in computer vision have significantly increased their robustness.

III. Data

MODIS data from the bands 1 (620–670 nm) and 2 (841–876) are selected for this study, as the ones with the highest available resolution (nominal 250 m, in practice 231.66 m). As in numerous studies [8], [12]–[14], daily composite images are employed. Daily composites may cause small blurring in sea ice floe edges, but since the best quality pixel from each swath is kept, they are less sensitive to cloud contamination and missing values compared with the single swath images. In particular, Level 2G atmospherically corrected images from the Terra satellite gridded into a sinusoidal map projection are used (MOD09GQ surface reflectance product) [37]. To cause no shape distortion to the sea ice objects in order to enhance motion estimation, as followed in similar studies [21], [31], [38], we reproject the data into a conformal projection, in particular a polar stereographic grid, tangent to the Earth's surface at 70 degrees northern latitude (Table I) [39]. The reprojection is performed with nearest-neighbor interpolation to keep the original intensity values intact and minimize potential edge smoothing. The genuine spatial resolution is kept intact, i.e., 231.66 m. The selected study area lies in the Eastern Beaufort Sea (Fig. 1), with its corner coordinates

TABLE I
PARAMETERS OF THE SELECTED POLAR STEREOGRAPHIC PROJECTION.

Projection parameters	
Ellipsoid	Hughes
Earth radius (km)	6378.273
Eccentricity	0.081816153
Standard parallel	70°N
Central Meridian	45°W

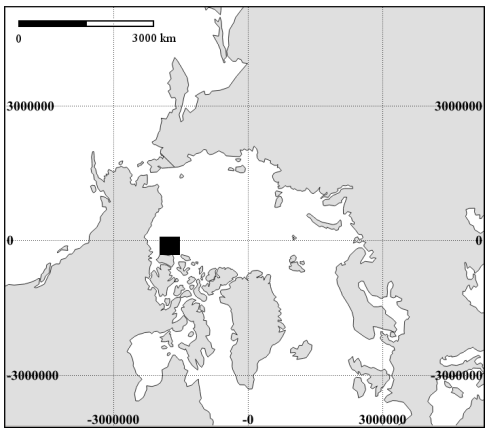

Fig. 1. The study area in the Eastern Beaufort Sea, indicated by a black rectangle, projected on a polar stereographic grid.

TABLE II
GEOGRAPHIC AND POLAR STEREOGRAPHIC COORDINATES OF THE CORNERS OF THE STUDY AREA AS (LATITUDE, LONGITUDE) PAIRS.

Corner	Geographic	Polar stereographic
Upper-left	(137°17′9″W, 72°1′44″N)	(–1960719,78265)
Upper-right	(137°57′20″W, 76°3′15″N)	(–1515939,78265)
Lower-left	(125°34′26″W, 71°48′4″N)	(–1960719,–325512)
Lower-right	(122°52′52″W, 75°45′29″N)	(–1515939,–325512)

drawn in Table II. A series of mainly clear-sky images from dates April 4–6 and 12–15, 2015, are selected to estimate sea ice motion.

Two kinds of masks are generated from MODIS products to enhance motion estimation, in particular an ocean mask for all dates and a pixel quality mask for each date. The former is produced from the state layer of the MODIS surface reflectance product of 1 km spatial resolution (MOD09GA) [40]. Pixels indicated as "shallow ocean," "continental/moderate ocean," and "deep ocean" in all dates are selected, in order to distinguish sea ice from land, coastlines, and inland water pixels. A pixel quality mask for each date is generated by concatenating i) a pixel quality mask from the 250 m MOD09GQ products, indicating pixels at ideal quality of capturing and geometric and atmospheric correction, and ii) a cloud-free and cloud-shadow-free mask from the 1 km MOD09GA products. The ocean and quality masks are re-projected to the grid and spatial resolution of the daily composite images.

IV. METHODS

A. Optical Flow

The proposed optical flow framework is based on the recently introduced computer vision approach for optical flow termed Edge-Preserving Interpolation of Correspondences (EpicFlow) [41]. The approach achieves competitive results even in cases of large displacements and significant occlusions. These are beneficial properties for a sea ice motion estimation framework to account for large drifts, due to either fast sea ice motion or lack of daily imagery, and for partial occlusions, e.g., due to cloud contamination or sea ice deformations.

As a first step of the framework, edge detection is performed in each MODIS image and band individually. The edge detection methodology proposed in [42] is followed here, demonstrating state-of-the-art results in low computational time, a highly desirable property for large remote sensing images. The approach faces edge detection as a structured learning problem. An image is split into patches and for each patch a local segmentation (edge) mask is produced by using random forests trained with appropriate structured labels. The local edge masks from all image patches are aggregated into the final edge mask with the same dimensions as the original image.

Before applying optical flow in an image pair, sparse correspondences between the two images are generated. The rationale is to provide initialization conditions to allow optical flow capture fast motions, since the matching correspondences can be arbitrarily distant in the two images, and increase its robustness to illumination changes, motion discontinuities, and occlusions. The approach proposed in [43] is followed, adopting a bottom-up multi-stage architecture with interleaving convolutions and max-pooling and with analogies to deep convolutional networks. The approach starts by splitting the first image in small non-overlapping patches and calculating the Scale Invariant Feature Transform (SIFT) descriptor [44]. Each patch is split in four quadrants (each of 2×2 pixels) and their best matching correspondences are searched in the second image, independently, thus allowing non-rigid matching. A response map is generated from the different similarity values arising from convolutions from the candidate locations and the local maximum is selected (max-pooling) for each patch. The patch size is increased by a factor of two and the process is repeated until reaching the dimensions of the image. The local maxima from each iteration are merged, favoring the ones from larger patches. In our case, due to memory constraints, the original patches are downsampled to half size. Sparse correspondences are produced, although with high density and implicit smoothness that facilitates the application of optical flow.

The sparse correspondences between an image pair, forming a set C, are then used by the optical flow approach to perform sparse-to-dense interpolation, i.e., generate dense correspondences. For an image pair, using the previously detected edges each pixel, p, of the first image not belonging to C is assigned to its closest pixel $p_c \in C$, based on a geodesic distance:

$$D(p, p_c) = \inf_{\Gamma \in P_{p,p_c}} \int_{\Gamma} E(p_s) \mathrm{d}p_s, \tag{5}$$

where P_{p,p_c} stands for all possible paths between pixels p and p_c, and $E(p_s)$ for the cost of crossing through a pixel p_s, which increases when crossing edges. For each correspondence $p_c \in C$, its nearest neighbors $p_n \in C$ identified and form a system of equations whose least square solution forms a locally-weighted affine estimation [45] of the distance of p_c to its correspondence in the second image. These affine transformation parameters are then used to estimate the distance, i.e., the correspondence, of each pixel $p \notin C$ assigned to p_c with its match in the second image. The resulting dense correspondences are used to initialize a variational energy minimization to calculate the final optical flow. The data term proposed in [46, eq. (27)], as robust under outliers and illumination variations, and the smoothness term in [47], with a local weight $a(\boldsymbol{x}) = \exp(-\kappa||\nabla_2 I(\boldsymbol{x})||)$. Here, $\boldsymbol{x}$ is the pixel coordinate and κ is set as 5.

As a final step, all calculated motion vectors with velocity more than 70 cm/sec per day are pruned to this maximum. As an example, for an image pair of consecutive days, any motion vector with 2-norm exceeding 60.48 km, or ≈261 pixels, is pruned to a magnitude of 60.48 km. This threshold is the one adopted by the NSIDC operational sea ice motion vector product and selected for consistency, since the latter is used for validation in this study (Section V).

B. Pattern Matching

A multi-resolution sea ice motion estimation approach using NCC and PC, as a popular choice in recent studies [20]–[22], [24], in particular mainly based on [22], is also implemented for comparison with the optical flow framework.

A multi-resolution image pyramid is first constructed from each of the available MODIS bands and dates. The image of the highest resolution is filtered by a 5×5 pixel median filtering. Then, for the construction of each new image pyramid level, a 5×5 pixel normal Gaussian filtering is applied [48], followed by a subsampling by 2 in both directions; thus, for each pyramid level, the image size is half than the previous one.

A *multi-cascade* approach is additionally followed, where in each cascade stage the size of the templates to be matched in the image pair is halved. The largest size of template is equal to the size of the coarsest resolution image in the pyramid. Given the size of the original images (1920×1743 pixels), the adopted restriction on the smallest template having at least 10×10 pixels to allow robust calculations, and the parameters in [22], we select a four-level pyramid and five-stage cascade scheme—with the largest template and the coarsest resolution image being 240×218 pixels. This results in a number of 128×128 non-overlapping templates of the smallest size within the image of the highest resolution.

For an image pair, at each cascade stage (i.e., templates of a certain size) and each pyramid level, a template in the first image, is compared with an equal-size template in the second, unless it has ≤10% of non-ocean or bad quality pixels, based on the quality masks (Section III), in which case it is flagged as missing. The PC matrix is calculated and the elements with values >25% of the maximum PC value, excluding 8-connected elements, are identified as candidate vectors indicating the relative motion between the two templates. Equation (2) is used to calculate the PC, adding 0.05 to the denominator to filter out frequencies with very low amplitudes. Candidate motion vectors that exceed the maximum magnitude of 60.48 km/day are discarded. For each of the rest vectors, the template in the second image is moved accordingly. For each of the vectors whose template in the second image includes <10% of non-ocean or bad quality pixels the NCC is calculated as in (1). The motion vector with the maximum NCC value is selected. As a note, motivated by similar studies [8], [27], we further evaluate two cut-off NCC thresholds, 0.6 or 0.3, below which the vector is flagged as missing. The experimental results with no threshold are more accurate, thus, no cut-off value is finally employed. After the vector selection, the template in the first image moves to the next location and the process is repeated, resulting, finally, in a field of motion vectors.

The process starts from the cascade stage with the maximum templates and the pyramid level with the coarsest resolution image. Then, it moves to the next pyramid level up to the last with the highest resolution image. The next cascade stage follows, i.e., the template size is halved, and the process restarts from the coarsest resolution image, until all cascade stage and pyramid level combinations are processed. At each stage-level step, the motion vectors from the previous step are inherited and refined. At the highest resolution level, the templates in the first image are non-overlapping, whereas for each next level the step between templates is halved to keep their number fixed for a certain cascade stage. At the final cascade stage and high-resolution pyramid level, 128×128 non-overlapping templates are formed, which is the number of the finally generated motion vectors.

Further processes to improve the accuracy of the motion vectors are applied after each cascade-level step. The consistency of each vectors with its neighbors is checked [8], [49]. In a neighborhood of 25×25 vectors, if the central vector has a magnitude or direction deviating by 4 standard deviations of the mean or 2 standard deviations of the median of magnitude or direction of the neighboring vectors, then it is flagged as missing. Then, a 3×3 vector median filtering is applied in vectors flagged as non-missing. Instead of an isotropic median filter in both directions independently, a median vector filtering as in [50] is adopted in our experiments. Finally, the missing vectors are interpolated with fifth-degree 2D Horner's polynomials [51].

V. Results

A. Validation Strategy

Although the most desirable way of validating sea ice motion vectors from remote sensing is the comparison with buoys, with position accuracy around 0.5 km/day [12], [13], there is no buoy data available in this study for the area of interest. Therefore, we compare the generated motion vectors with the operational sea ice motion vectors provided by NSIDC, in particular the gridded Polar Pathfinder daily 25 km EASE-Grid (Equal-Area Scalable Earth Grid) sea ice motion vectors version 3 product [13]. The vectors are produced by

fusion of buoy, AVHRR, and passive microwave data, have a spatial resolution of 25 km, and are distributed in a gridded format covering the entire Arctic, thus, providing an adequate number of vectors in our selected area for statistical analysis. Although the NSIDC grid vectors are subject to errors, with the root-mean-squared errors (RMSE) of the vectors from the individual sensors ranging between 3.29 cm/sec and 5.24 cm/sec [13], i.e., around 3–4 km/day, they are employed in this study as means to evaluate the consistency and the degree of correlation of the generated motion vectors with an operational product. In line with the validation strategy in previous studies [12], [14], the closest motion vector from the pattern matching method is selected for each NSIDC grid vector in the study area. For direct comparison, the optical flow vector with origin in the same location as the pattern matching one is selected as well.

B. Optical Flow and Pattern Matching Comparison

Motion vectors are estimated for the six image pairs of consecutive dates, i.e., five pairs of one-day interval and one pair of six-day interval (Section III) from each MODIS band separately.

Figure 2 draws an example of the motion vectors generated by the optical flow ("Flow") and the pattern matching ("MCC") approaches, using the MODIS band 2 products from April 4 and 5. The results for the full study area are shown on top for the two approaches, together with the respective grid data used for validation ("Grid"). On a broad scale, the motion vectors from both approaches seem to correlate similarly well with the grid data. However, some close-up instances, e.g., from the lower-right corner of the area shown in Fig. 2c and 2d, show some cases where the MCC vectors tend to have significantly larger magnitude or deviations in direction compared with the reference data.

Table III provides a number of statistical evaluation measures from the comparison between the optical flow and pattern matching vectors with the reference NSIDC grid data, for all six image pairs of MODIS band 2. In particular, the relative squared error (RSE), root mean-squared error (RMSE), mean-absolute error (MAE), and the Pearson correlation coefficient [52] are calculated for the drifts in both x and y axes. In all accuracy measures the motion vectors from the optical flow approach correlate with the grid data significantly higher than the pattern matching vectors do. As an indicative example, the RMSE of pattern matching vectors on the x axis is more than double the one of optical flow. On the contrary, optical flow vectors on the same axis reach almost a perfect correlation (P = 0.952) with the grid data. Optical flow vectors approach the grid data more closely on the x axis than the y axis, whereas this difference is not so notable in pattern matching vectors.

The aforementioned results are schematically represented by the scatterplots between the optical flow or pattern matching and the reference grid data drawn in Fig. 3. In line with the accuracy measures in Table III, the optical flow motion vectors correlate with the NSIDC grid data vectors higher than the pattern matching ones. In particular, the former vectors lie closer to the ideal one-by-one fitting line ("baseline"), with

TABLE III
OVERALL ACCURACY EVALUATION OF THE OPTICAL FLOW ("FLOW") AND PATTERN MATCHING ("MCC") VECTORS, FOR ALL SIX IMAGE PAIRS OF MODIS BAND 2 DATA, THROUGH RELATIVE SQUARED ERROR (RSE), ROOT MEAN-SQUARED ERROR (RMSE), MEAN-ABSOLUTE ERROR (MAE), AND THE PEARSON CORRELATION COEFFICIENT.

		Flow	MCC
	# vectors	1522	1522
δx	RSE	**0.245**	1.174
	RMSE (km)	**5.705**	12.494
	MAE (km)	**2.875**	4.398
	P	**0.952**	0.450
δy	RSE	**6.163**	9.605
	RMSE (km)	**8.121**	10.138
	MAE (km)	**4.724**	5.462
	P	**0.609**	0.425

TABLE IV
MEAN AND STANDARD DEVIATION OF THE ERROR DISTRIBUTIONS OF THE OPTICAL FLOW AND PATTERN MATCHING VECTORS FROM ALL IMAGE PAIRS OF MODIS BAND 2 DATA, FOR THE X AND Y DIRECTIONS.

	Flow	MCC
# vectors	1522	1522
μ_x	–2.027	0.353
σ_x	5.335	12.493
μ_y	–4.449	–3.370
σ_y	6.796	9.565

significantly less outliers than the latter vectors. As noticed, the reference NSIDC vectors indicate motions mainly towards the negative directions of the x and y axes. Optical flow vectors (Fig. 3a and 3b) follow the same direction, in general, although with a tendency to overestimate the reference motion magnitude. Besides a process error, another possible explanation may be that the ≈250 m high resolution MODIS vectors can capture small extent motion, e.g., of some hundreds of meters or few kilometers, that is undetected by the NSIDC 25 km coarse resolution data. The same tendency appears in the pattern matching vectors (Fig. 3c and 3d). However, several vectors estimate motion on opposite direction than the reference vectors, as seen from the vectors on the upper left quadrant of the scatterplot, especially for the x-axis motion (Fig. 3c).

Fig. 4 draws the error distributions for the optical flow and pattern matching vectors from all image pairs of MODIS band 2 data, calculated as the difference of the measured and the NSIDC grid vectors at each axis, together with histograms of their probability density functions (pdfs). The respective mean and standard deviation values of the pdfs are given in Table IV. The aforementioned outliers of the pattern matching approach are obvious in Fig. 4b, whereas errors of the optical flow vectors are less variant. In fact, although optical flow vectors appear slightly more biased than the pattern matching vectors, the standard deviation of the latter is significantly higher than the former ones, as a result of the existing extreme errors.

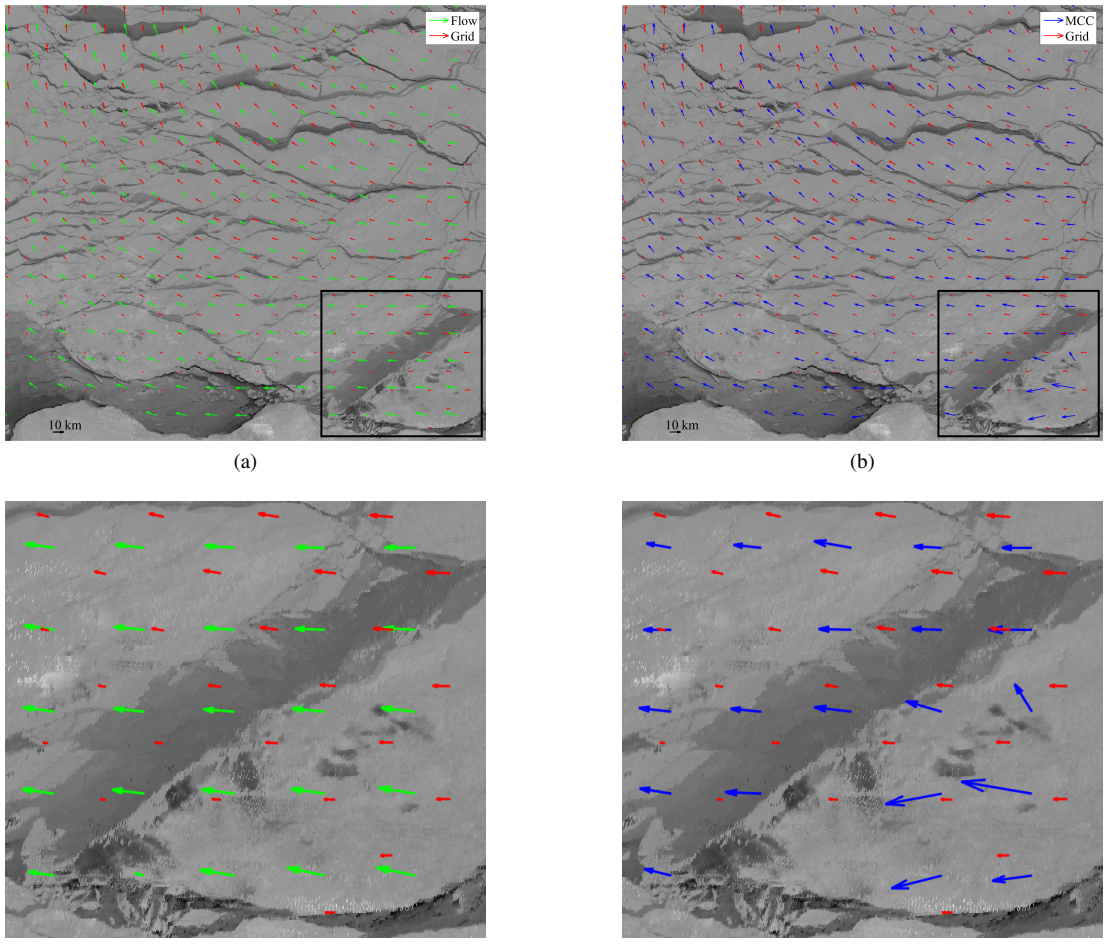

Fig. 2. Motion vectors generated by the optical flow ("Flow") and the pattern matching ("MCC") approaches, using the MODIS band 2 products from April 4 and 5, together with the respective grid data used for validation ("Grid"). The results for the entire study are shown on the top, whereas a close-up look from the area within the black rectangle is shown on the bottom.

C. Large displacements

One of the tested image pairs is between April 6 and 12, i.e., having a six-day interval. This proved useful in assessing the results of the two approaches on large displacements. Additionally, it served as indication of the potential to estimate vectors when images from some dates are unavailable. Fig. 5 draws the motion vectors from optical flow and pattern matching, for MODIS band 2 images. As readily seen the magnitude of the vectors is significantly larger than one-day interval motions (Fig. 2). Optical flow vectors seem to correlate highly with the vectors from the reference grid data (Fig. 5a). On the contrary, vectors of extreme differences with the reference ones in both magnitude and direction are generated by the pattern matching method. Such extreme outliers are obvious mainly in the upper mid and the lower right part of the image. In particular, the error values for the optical flow vectors, compared with the reference data for both axes, are significantly lower than the pattern matching vectors. Indicatively, the RMSE for the x axis is 13.28 km for the optical flow and 30.35 km for pattern matching, whereas the respective RMSE values for the y axis are 18.09 km and 23.52 km, respectively. In general, both approaches seem to overestimate the magnitude of the vectors compared with the reference data, particularly in the mid part of the image, which might be related up to a degree to the quantization restrictions of the 25 km coarse resolution of the reference data. However, the direction of the generated vectors in this part is highly correlated with the reference vectors. Overall, the optical flow method appears able to capture even large displacements more accurately than the pattern matching approach, mainly assisted by the sparse correspondences generated at the beginning of the process.

D. Experiments With Data Variations

We further evaluate the potential of the two methods under different variations of the MODIS input data. In particular, filtering processes employed in previous studies are applied to both the band 1 and 2 MODIS datasets. More specifically, similar to the construction of the image pyramid for the pattern matching method [20], [22], a 5×5 median filtering is applied to the original images, followed by an optional 5×5 normal Gaussian filtering [20], [22]–[24]. Alternatively, a 5×5 Laplacian filtering is also applied to the original MODIS images [8], [14]. The evaluation results for the entire six-pair

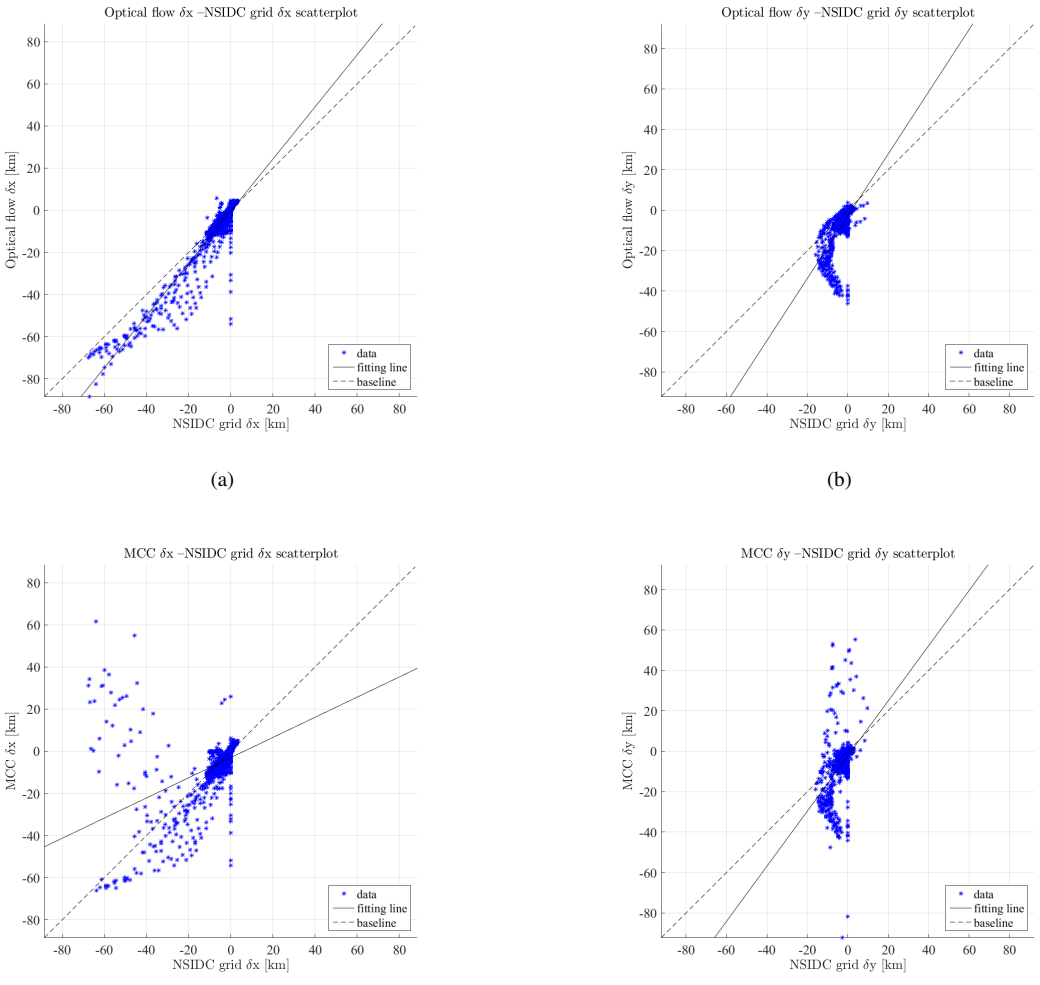

(a) (b)

(c) (d)

Fig. 3. Scatterplots of the optical flow (top) and pattern matching (bottom) vectors from the MODIS band 2 data against the reference NSIDC grid vectors at the x and y directions, for all six image pairs. The dashed line represents the ideal one-by-one correlation, whereas the solid line the estimated fitting line through least squares linear regression.

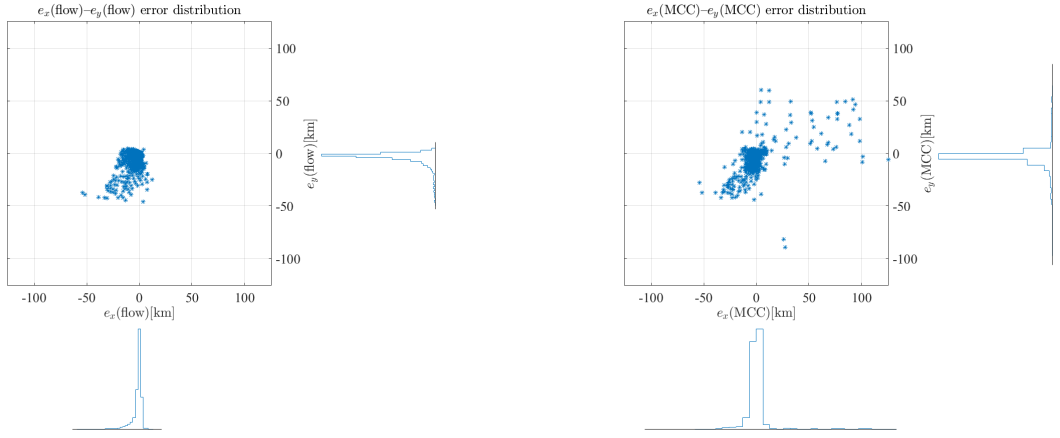

(a) (b)

Fig. 4. Error distributions for the optical flow and pattern matching vectors from all image pairs of MODIS band 2 data, calculated as the difference of the measured and the NSIDC grid vectors at each axis, together with histograms of the error probability density functions.

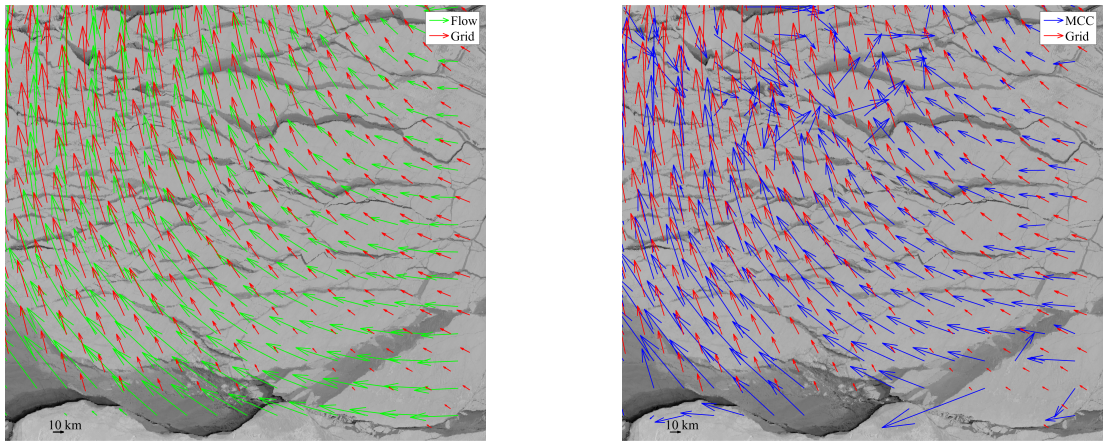

(a) (b)

Fig. 5. Motion vectors generated by the optical flow ("Flow") and the pattern matching ("MCC") approaches, using the MODIS band 2 products from April 6 and 12, together with the respective grid data used for validation ("Grid").

datasets of each data version are reported in Table V. For brevity, instead of the motions in each direction individually, the accuracy on the estimated motion magnitude is provided. We observe that the optical flow method outperforms pattern matching for almost all data inputs consistently, i.e., under all accuracy measures. The only exception occurs when Laplacian filtering is first applied in the MODIS images. Laplacian filtering tends to highlight or create artificial edges in the images, often over-segmenting sea ice objects, which create confusion to the sparse correspondences generated and propagated to the optical flow core approach. Experiments with restricting the search space in a close neighborhood during the sparse correspondence matching significantly improve the results; these are not reported here, though, for the sake of consistency. About the pre-processing methods, the vectors generated from the original images ("B1" and "B2") correlate with the reference data better than the vectors from the pre-processed data. In general, the band 2 data versions provide more accurate results overall, although the band 1 versions seem to slightly outperform the band 2 ones specifically for optical flow. As a side note, the different number of vectors among the versions is due to the generation by the pattern matching method of motion vectors that end at templates where more than 10% of the pixels are non-ocean or of bad quality and they are considered as missing.

TABLE V
EVALUATION OF OPTICAL FLOW AND PATTERN MATCHING VECTORS WITH DIFFERENT VERSIONS OF THE MODIS INPUT DATA, FOR ALL SIX IMAGE DATE PAIRS. IN PARTICULAR, USING THE ORIGINAL BAND 1 ("B1") AND BAND 2 ("B2") IMAGES, OR APPLYING MEDIAN ("MED"), MEDIAN AND GAUSSIAN ("MED+GAUSS"), OR LAPLACIAN ("LAPL") FILTERING.

Versions	# vectors	RSE	RMSE	MAE	P
Flow					
B1	1512	**0.68**	**9.42**	**5.42**	**0.88**
B1+Med	1514	**0.66**	**9.25**	**5.30**	**0.87**
B1+Med+Gauss	1518	**0.67**	**9.36**	**5.37**	**0.87**
B1+Lapl	1511	20.99	51.34	49.57	-0.27
B2	1522	**0.69**	**9.49**	**5.47**	**0.88**
B2+Med	1524	**0.74**	**9.77**	**5.54**	**0.87**
B2+Med+Gauss	1522	**0.72**	**9.71**	**5.53**	**0.87**
B2+Lapl	1522	103.51	114.40	84.10	0.57
MCC					
B1	1512	3.52	21.41	8.96	0.77
B1+Med	1514	4.18	23.27	9.60	0.76
B1+Med+Gauss	1518	7.48	31.17	11.56	0.73
B1+Lapl	1511	**1.08**	**11.63**	**6.14**	**0.67**
B2	1522	0.87	10.69	5.87	0.71
B2+Med	1524	1.18	12.36	6.34	0.74
B2+Med+Gauss	1522	1.78	15.31	6.97	0.76
B2+Lapl	1522	**1.07**	**11.61**	**6.18**	**0.69**

VI. DISCUSSION

In the experiments described in this study, the sea ice motion vectors from the proposed optical flow framework highly correlate with the reference vectors. Our framework consistently outperforms the state-of-the-art pattern matching approach used for comparison in all image pairs, of both single-day and multi-day intervals, as well as in most versions of input data. Contrary to the common notion in previous studies [20], aided by the coarse matching step, the optical flow method can capture both small and large displacements more accurately than the pattern matching approach. Fig. 6 draws an example of the sparse correspondences generated at the beginning of the optical flow framework. As observed in Fig. 6b, where all pairwise correspondences are shown, their number is rather high, covering the largest part of the images. These quasi-dense matches seem to provide a particularly beneficial initialization to the optical flow approach. Although specific matching pairs cannot be distinguished in Fig. 6b, the color distribution of the cross marks—each hue and saturation value representing a pairwise correspondence in the two images—appears very similar in the two images. This indicates that pixel matches are spatially consistent and supports that the pyramid structure of the match searching

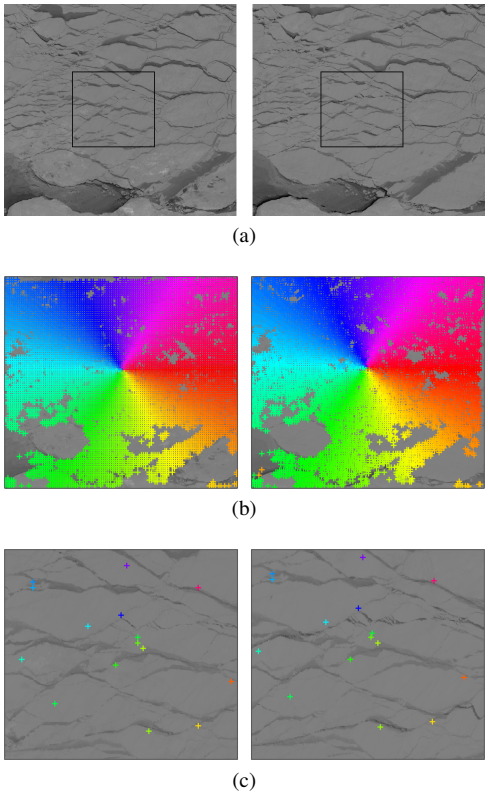

Fig. 6. Sparse correspondences between images from April 4 (left) and 5 (right), 2015. (a) The original MODIS band 2 images. (b) All sparse correspondences from the 5×5 median filtered MODIS band 2 images. Cross marks of the same color indicate corresponding pixels between the two images. (c) Close-up look of the correspondences in (b) from the area within the black rectangle shown in (a). Only 1% of the total correspondences are shown to make the cross marks visually distinct.

algorithm enhances the smoothness of the estimated motion. Fig. 6c offers a close-up look of a selected area, where specific pixel correspondences can be observed (only 1% of the correspondences in the area is shown). It is noteworthy that matches are found not only in distinct edges, but also in positions with less intense image gradients.

Besides the advantage of accuracy, two additional properties of the proposed optical flow framework favor its use in sea ice motion estimation over the pattern matching framework. Optical flow produces a dense motion vector field, where a vector is calculated for each pixel of the original image, i.e., the vector field has the same resolution as the original image. This is important for local scale applications, such as navigation, as well as modeling and prediction applications where multiple observation data are desirable. On the contrary, pattern matching approaches face the templates as regions with homogeneous motions, and besides failing to capture local non-rigid deformations, they usually provide a single motion vector for the entire template, thus the motion vector field has coarser resolution than the employed data. A second advantageous property of the optical flow framework, in line with the expectations from previous studies [18], is that it is more computationally efficient than the pattern matching approach. In particular, on a four-core Intel® Xeon® CPU E5506 at 2.13 GHz used in this study, the generation of the motion vectors for a single image pair takes less than six minutes with the optical flow framework, among which the edge detection, sparse matching, and optical flow interpolation and minimization parts take ≈19 sec, 5 min 13 sec, and 18 sec, respectively. On the other side, the pattern matching method requires approximately 28 min to process an image pair, although the multi-resolution approach and the use of phase correlation pre-selection are specifically included to decrease its computational cost.

In combination with the optical flow framework, MODIS data showed potential in generating motion vectors that combine a spatial resolution similar to SAR data and a daily frequency equal to passive microwave data. The MODIS data are subject to the optical sensor limitations, as AVHRR, requiring clear-sky conditions and sun illumination of the study area. This may heavily restrict their availability in the Arctic due to intense cloud presence throughout the year, and even more in areas close to the North Pole during the winter months due to the lack of sun illumination. However, as shown in the experiment results, the motion is effectively estimated even for a six-day interval MODIS image pair. This result demonstrates the potential of the MODIS data and optical flow framework to overcome the unavailability of images from a certain number of days between two non-consecutive available dates, even if some large displacements and non-rigid transformations are present during this period. A properly selected interpolation method could be applied in such cases to estimate the motion during the non-available dates. This study does not necessarily promote the use of MODIS data as alternative to widely employed passive microwave and SAR. Instead, it aims at highlighting the high potential of MODIS data in providing large extent motion vector fields at high spatial resolution and even in non-consecutive days. This potential has been underestimated by previous studies. MODIS can be used in tandem with other sensors to improve the spatial and/or temporal resolution of research or operational products.

It is worth noting that the 25 km coarse resolution NSIDC operational motion vector products are mainly used to assess the consistency of the generated vectors throughout the data grid. In fact, as demonstrated in a close-up look example of the generated motion vectors from the April 4–5 pair shown in Fig. 7, several real motions are underestimated by the coarse resolution NSIDC data. The figure draws the same vectors using the April 4 (Fig. 7a) and 5 (Fig. 7b) image as background, to show the real starting and ending positions of the motion vectors. The ice drift from the NSIDC data is calculated by multiplying the average velocity between April 4 and 5, given by NSIDC, by this one-day time interval. As seen, motion vectors generated by the optical flow framework capture the true displacements in higher accuracy than the reference NSIDC data, possibly due to the higher resolution of the MODIS data. Thus, this observation may suggest that the true error from the optical flow—and similarly from the pattern matching method—is less than reported in the experiments. However, for the majority of the vectors, the magnitude, and even more, the direction of the vectors align well with the visually inspected image displacements. This suggests the suitability of the NSIDC grid to assess the consistency, and

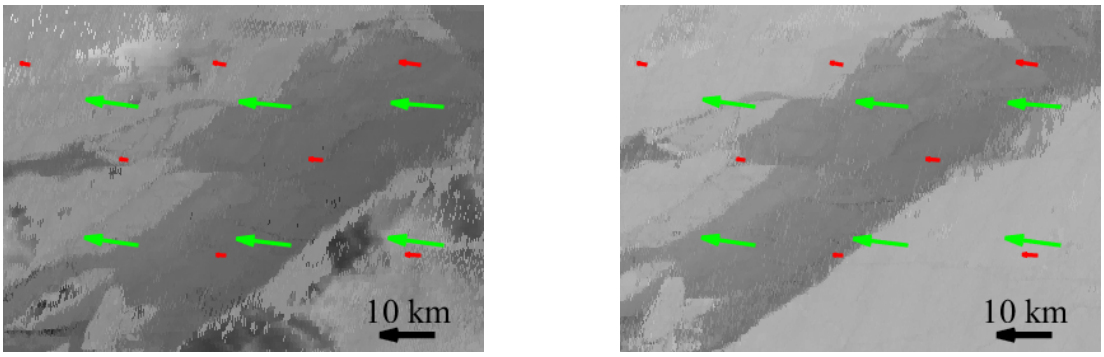

(a) (b)

Fig. 7. Close-up look from the optical flow and NSIDC grid motion vectors for the MODIS band 2 image pair between April 4 and 5. The same vectors are drawn, with the images from (a) April 4 and (b) April 5 as background. The vectors are drawn in the scale of the image.

up to a degree, the accuracy of the motion vectors generated in this study, under the lack of buoy observations.

VII. Conclusion

In this study, a framework based on optical flow is proposed for sea ice motion estimation using high resolution MODIS daily reflectance data. The framework is compared with a state-of-the-art multi-resolution pattern matching method based on normalized cross-correlation and phase correlation. Six image pairs are employed in the experiments, including both single- and multi-day interval imagery. The optical flow method consistently outperforms the pattern matching approach, showing higher correlation with a coarse resolution operational motion vector product used for reference. The optical flow method provides a dense motion vector field, contrary to the sparse vector field by the pattern matching approach. Optical flow proves more able to capture accurately both small and large displacements, more robust to input data variations, and more computationally efficient than its pattern matching counterpart. The results make the wider applicability of optical flow in sea ice motion studies promising. In addition, MODIS optical data proves effective in motion estimation at high spatial resolution, both with daily and multi-day-interval images. This suggests MODIS potential for research and operational use, either alone or in fusion with other satellite sensors.

Acknowledgment

The authors would like to thank Yuancheng Ye for his valuable assistance during the preparation of the optical flow experiments.

References

[1] T. Kræmer, H. Johnsen, and C. Brekke, "Emulating Sentinel-1 Doppler radial ice drift measurements using Envisat ASAR data," *IEEE Trans. Geosci. Remote Sens.*, vol. 53, no. 12, pp. 6407–6418, Dec. 2015.

[2] L. W. A. De Silva, H. Yamaguchi, and J. Ono, "Ice–ocean coupled computations for sea-ice prediction to support ice navigation in Arctic sea routes," *Polar Res.*, vol. 34, Nov. 2015, 25008.

[3] N. Kimura, A. Nishimura, Y. Tanaka, and H. Yamaguchi, "Influence of winter sea-ice motion on summer ice cover in the Arctic," *Polar Res.*, vol. 32, Nov. 2013, 20193.

[4] W. N. Meier, J. A. Maslanik, and C. W. Fowler, "Error analysis and assimilation of remotely sensed ice motion within an Arctic sea ice model," *J. Geophys. Res.*, vol. 105, pp. 3339–3356, Feb. 2000.

[5] S. J. Hassol, "Impacts of a Warming Arctic," Arctic Climate Impact Assessment, Cambridge, United Kingdom, Tech. Rep., 2004.

[6] G. Spreen, R. Kwok, and D. Menemenlis, "Trends in arctic sea ice drift and role of wind forcing: 1992–2009," *Geophys. Res. Lett.*, vol. 38, no. 19, Oct. 2011, l19501.

[7] J. Askne and W. Dierking, "Sea ice monitoring in the arctic and baltic sea using SAR," in *Remote Sensing of the European Seas*, V. Barale and M. Gade, Eds. Dordrecht, Netherlands: Springer Netherlands, 2008, ch. 3, pp. 383–398.

[8] F. Girard-Ardhuin and R. Ezraty, "Enhanced arctic sea ice drift estimation merging radiometer and scatterometer data," *IEEE Trans. Geosci. Remote Sens.*, vol. 50, no. 7, pp. 2639–2648, Jul. 2012.

[9] W. J. Emery, C. Fowler, and J. A. Maslanik, "Satellite-derived maps of Arctic and Antarctic sea-ice motion: 1988 to 1994," *Geophys. Res. Letters*, vol. 24, no. 8, pp. 897–900, Apr. 1997.

[10] R. Kwok, D. A. Schweiger, D. A. Rothrock, S. Pang, and C. Kottmeier, "Sea ice motion from satellite passive microwave imagery assessed with ERS SAR and buoy motions," *J. Geophys. Res.*, vol. 103, no. C4, pp. 8191–8214, Apr. 1998.

[11] W. N. Meier and J. A. Maslanik, "Effect of environmental conditions on observed, modeled, and assimilated sea ice motion errors," *J. Geophys. Res.*, vol. 108, no. C5, May 2003, 3152.

[12] W. N. Meier and M. Dai, "High-resolution sea-ice motions from AMSR-E imagery," *Ann. Glaciol.*, vol. 44, pp. 352–356, Nov. 2006.

[13] M. Tschudi, C. Fowler, J. Maslanik, J. S. Stewart, and W. Meier, "Polar Pathfinder daily 25 km EASE-Grid sea ice motion vectors, version 3, Daily Grids," Boulder, Colorado USA: NASA National Snow and Ice Data Center Distributed Active Archive Center, 2016. doi: http://dx.doi.org/10.5067/O57VAIT2AYYY. Accessed on: Jul. 14, 2016.

[14] T. Lavergne, S. Eastwood, Z. Teffah, H. Schyberg, and L. A. Breivik, "Sea ice motion from low-resolution satellite sensors: An alternative method and its validation in the Arctic," *J. Geophys. Res.*, vol. 115, Oct. 2010.

[15] Y. Zhao, A. K. Liu, and D. G. Long, "Validation of sea ice motion from QuikSCAT with those from SSM/I and buoy," *IEEE Trans. Geosci. Remote Sens.*, vol. 40, no. 6, pp. 1241–1246, Jun. 2002.

[16] S. Gutiérrez and D. G. Long, "Optical flow and scale-space theory applied to sea-ice motion estimation in Antarctica," in *IEEE Int. Geoscience and Remote Sensing Congr.*, vol. 4, 2003, pp. 2805–2807.

[17] J. Haarpaintner, "Arctic-wide operational sea ice drift from enhanced-resolution QuikScat/SeaWinds scatterometry and its validation," *IEEE Trans. Geosci. Remote Sens.*, vol. 44, no. 1, pp. 102–107, Jan. 2006.

[18] Y. Sun, "Automatic ice motion retrieval from ERS-1 SAR images using the optical flow method," *Int. J. Remote Sens.*, vol. 17, no. 11, pp. 2059–2087, 1996.

[19] M. Leppäranta, Y. Sun, and J. Haapala, "Comparisons of sea-ice velocity fields from ERS-1 SAR and a dynamic model," *J. Glaciol.*, vol. 44, no. 147, pp. 248–262, 1998.

[20] M. Thomas, C. A. Geiger, and C. Kambhamettu, "High resolution (400 m) motion characterization of sea ice using ERS-1 SAR imagery," *Cold Reg. Sci. Technol.*, vol. 52, pp. 207–223, Apr. 2008.

[21] M. Thomas, C. Kambhamettu, and C. A. Geiger, "Motion tracking of discontinuous sea ice," *IEEE Trans. Geosci. Remote Sens.*, vol. 49, no. 12, pp. 5064–5079, Dec. 2011.
[22] T. Hollands and W. Dierking, "Performance of a multiscale correlation algorithm for the estimation of sea-ice drift from SAR images: Initial results," *Ann. Glaciol.*, vol. 52, no. 57, pp. 311–317, May 2011.
[23] J. Karvonen, "Operational SAR-based sea ice drift monitoring over the Baltic Sea," *Ocean Sci.*, vol. 8, no. 4, pp. 473–483, Jul. 2012.
[24] A. S. Komarov and D. G. Barber, "Sea ice motion tracking from sequential dual-polarization RADARSAT-2 images," *IEEE Trans. Geosci. Remote Sens.*, vol. 52, no. 1, Jan. 2014.
[25] A. Berg and L. E. B. Eriksson, "Investigation of a hybrid algorithm for sea ice drift measurements using Synthetic Aperture Radar images," *IEEE Trans. Geosci. Remote Sens.*, vol. 52, no. 8, pp. 5023–5033, Aug. 2014.
[26] R. M. Ninnis, W. J. Emery, and M. J. Collins, "Automated extraction of pack ice motion from advanced very high resolution radiometer imagery," *J. Geophys. Res.*, vol. 91, no. C9, pp. 10 725–10 734, Sep. 1986.
[27] W. J. Emery, C. W. Fowler, J. Hawkins, and R. H. Preller, "Fram Strait satellite image-derived ice motions," *J. Geophys. Res.*, vol. 96, no. C3, pp. 4751–4768, Mar. 1991.
[28] J. A. Leese, C. S. Novak, and B. B. Clark, "An automated technique for obtaining cloud motion from geosynchronous satellite data using cross correlation," *J. Appl. Meteorol.*, vol. 10, pp. 118–132, Feb. 1971.
[29] J. Gao and M. B. Lythe, "The maximum cross-correlation approach to detecting translational motions from sequential remote-sensing images," *Comput. Geosci.*, vol. 22, no. 5, pp. 525–529, Jun. 1996.
[30] W. Chen, "Current motion tracking from satellite image sequence with global similarity optimization model," *IEEE Trans. Geosci. Remote Sens.*, vol. 53, no. 2, pp. 1008–1015, Feb. 2015.
[31] R. Kwok, J. C. Curlander, R. McConnell, and S. S. Pang, "An ice-motion tracking system at the Alaska SAR facility," *IEEE J. Ocean. Eng.*, vol. 15, no. 1, pp. 44–54, Jan. 1990.
[32] D. Fleet and Y. Weiss, "Optical flow estimation," in *Handbook of Mathematical Models in Computer Vision*, N. Paragios, Y. Chen, and O. Faugeras, Eds. New York, NY: Springer, 2006, ch. 15, pp. 239–257.
[33] A. Wedel and D. Cremers, "Optical flow estimation," in *Stereo Scene Flow for 3D Motion Analysis*. London, United Kingdom: Springer, 2011, ch. 2, pp. 5–34.
[34] B. D. Lucas and T. Kanade, "An iterative image registration technique with an application to stereo vision," in *Proc. 7th Int. Joint Conf. Artificial Intelligence*, vol. 2, 1981, pp. 674–679.
[35] S. Baker and I. Matthews, "Lucas-Kanade 20 years on: A unifying framework," *Int. J. Comp. Vision*, vol. 56, no. 3, pp. 221–255, Feb. 2004.
[36] B. K. B. Horn and B. G. Schunck, "Determining optical flow," *Artif. Intell.*, vol. 17, no. 1-3, pp. 185–203, Aug. 1981.
[37] E. Vermote and R. Wolfe, "MOD09GQ MODIS/Terra surface reflectance daily L2G global 250m SIN grid v006," NASA EOSDIS Land Processes DAAC, 2015. Doi: http://doi.org/10.5067/MODIS/MOD09GQ.006.
[38] J. Mouginot, B. Scheuchl, and E. Rignot, "Mapping of ice motion in Antarctica using Synthetic-Aperture Radar data," *Remote Sens.*, vol. 4, no. 9, pp. 2753–2767, Sep. 2012.
[39] National Snow and Ice Data Center, "Documentation: Polar stereographic projection and grid," [Online]. Available: http://nsidc.org/data/polar-stereo/ps_grids.html, Accessed on: Jul. 18, 2016.
[40] E. Vermote and R. Wolfe, "MOD09GA MODIS/Terra surface reflectance daily L2G global 1km and 500m SIN grid v006," NASA EOSDIS Land Processes DAAC, 2015. Doi: http://doi.org/10.5067/MODIS/MOD09GA.006.
[41] J. Revaud, P. Weinzaepfel, Z. Harchaoui, and C. Schmid, "EpicFlow: Edge-preserving interpolation of correspondences for optical flow," in *IEEE Conf. Computer Vision and Pattern Recognition*, 2015, pp. 1164–1172.
[42] P. Dollár and C. L. Zitnick, "Fast edge detection using structured forests," *IEEE Trans. Pattern Anal. Mach. Intell.*, vol. 37, no. 8, pp. 1558–1570, Aug. 2015.
[43] P. Weinzaepfel, J. Revaud, Z. Harchaoui, and C. Schmid, "DeepFlow: Large displacement optical flow with deep matching," in *IEEE Int. Conf. Computer Vision*, 2013, pp. 1385–1392.
[44] R. Szeliski, *Computer Vision: Algorithms and Applications*. London, United Kingdom: Springer, 2011.
[45] R. I. Hartley and A. Zisserman, *Multiple View Geometry in Computer Vision*, 2nd ed. Cambridge, United Kingdom: Cambridge University Press, 2004.
[46] H. Zimmer, A. Bruhn, and J. Weickert, "Optic flow in harmony," *Int. J. Comput. Vision*, vol. 93, no. 3, pp. 368–388, Jul. 2011.
[47] L. Xu, J. Jia, and Y. Matsushita, "Motion detail preserving optical flow estimation," *IEEE Trans. Pattern Anal. Mach. Intell.*, vol. 34, no. 9, pp. 1744–1757, Sep. 2012.
[48] M. Petrou and C. Petrou, *Image Processing : The Fundamentals*, 2nd ed. Chichester, United Kingdom: John Wiley & Sons, 2010.
[49] R. Ezraty, F. Girard-Ardhuin, and J. Piollé, "Sea ice drift in the central Arctic estimated from SeaWinds/QuikSCAT backscatter maps: User's manual," IFREMER, Brest, France, Version 2.2, 2007.
[50] J. Astola, P. Haavisto, and Y. Neuvo, "Vector median filters," *Proc. IEEE*, vol. 78, no. 4, pp. 678–689, Apr. 1990.
[51] P. Borwein and T. Erdélyi, *Polynomials and Polynomial Inequalities*. New York, NY: Springer, 1995.
[52] I. H. Witten, E. Frank, and M. A. Hall, *Data Mining: Practical Machine Learning Tools and Techniques*, 3rd ed. Burlington, MA: Morgan Kaufmann, 2011.

Zisis I. Petrou (S'05–M'15) received the Diploma in electrical and computer engineering from the Aristotle University of Thessaloniki, Greece, in 2007 and the M.Sc. degree in space studies from the International Space University, Strasbourg, France, in 2009. In 2015, he received the Ph.D. degree in remote sensing from the Department of Electrical and Electronic Engineering, Imperial College London, United Kingdom.

In 2009, he was an Intern with the German Aerospace Center (DLR), Oberpfaffenhofen, Germany. From 2009 to 2016, he was a Research Assistant with the Centre for Research and Technology Hellas, Thessaloniki, Greece. Since February 2016, he has been a Postdoctoral Research Scholar with the City College of New York, City University of New York. His research interests include classification, motion detection and prediction analysis on remote sensing images using advanced machine learning, image processing, and computer vision techniques.

Dr. Petrou is a member of the Technical Chamber in Greece. He was the recipient of the Best Paper Award for Young Professionals under 35 at the 2nd International Conference on Space Technology, Athens, in 2011, sponsored by IEEE. He has been a scholar of the European Space Agency (ESA) and the Onassis Foundation, Greece.

YingLi Tian (M'99–SM'01) received the B.S. and M.S. degrees from Tianjin University, China, in 1987 and 1990, and the Ph.D. degree from Chinese University of Hong Kong, Hong Kong, in 1996.

After holding a faculty position at National Laboratory of Pattern Recognition, Chinese Academy of Sciences, Beijing, she joined Carnegie Mellon University in 1998, where she was a postdoctoral fellow at the Robotics Institute. She then worked as a research staff member in IBM T. J. Watson Research Center from 2001 to 2008. She is one of the inventors of the IBM Smart Surveillance Solutions. She is currently a professor in the Department of Electrical Engineering at City College and Graduate Center, City University of New York. Her current research focuses on a wide range of computer vision problems from motion detection and analysis, assistive technology, to facial expression analysis, human action recognition, and video surveillance.